Title
CONVECTIVE BURSTS AND THE COUPLING OF SATURN'S EQUATORIAL STORMS AND INTERIOR ROTATION

Journal
The Astrophysical Journal, 746(1)

ISSN
0004-637X

Authors
Heimpel, Moritz
Aurnou, Jonathan M

Publication Date
2012-02-10

DOI
10.1088/0004-637x/746/1/51

Peer reviewed

The Astrophysical Journal, 746:51 (14pp), 2012 February 10 doi:10.1088/0004-637X/746/1/51

CONVECTIVE BURSTS AND THE COUPLING OF SATURN'S EQUATORIAL STORMS AND INTERIOR ROTATION

Moritz Heimpel[1] and Jonathan M. Aurnou[2]
[1] Department of Physics, University of Alberta, Edmonton, Alberta T6G 2J1, Canada; mheimpel@ualberta.ca
[2] Department of Earth and Space Sciences, University of California, Los Angeles, CA, USA; aurnou@ucla.edu
Received 2011 March 29; accepted 2011 November 21; published 2012 January 24

ABSTRACT

Temporal variations of Saturn's equatorial jet and magnetic field hint at rich dynamics coupling the atmosphere and the deep interior. However, it has been assumed that rotation of the interior dynamo must be steady over tens of years of modern observations. Here we use a numerical convection model and scaling estimates to show how equatorial convective bursts can transfer angular momentum to the deeper interior. The numerical model allows angular momentum transfer between a fluid outer spherical shell and a rigid inner sphere. Convection drives a prograde equatorial jet exhibiting quasiperiodic bursts that fill the equatorial volume outside the tangent cylinder. For each burst strong changes in the equatorial surface velocity are associated with retrograde torque on the inner sphere. Our results suggest that Saturn's Great White Spot, a giant storm that was observed to fill the equatorial region in 1990, could mobilize a volume of fluid carrying roughly 15% of Saturn's moment of inertia. Conservation of angular momentum then implies that a 20% change in the equatorial jet angular velocity could change the average interior rotation rate by about 0.1%—roughly an order of magnitude less than the apparent rotation rate changes associated with Saturn's kilometric radio (SKR) signal. However, if the SKR signal originates outside the liquid metal core in a "planetary tachocline" that separates the layer of fast zonal flow from the magnetically controlled and slowly convecting deep interior, then convective bursts can provide a possible mechanism for the observed ∼1% SKR changes.

Key words: convection – planets and satellites: individual (Saturn, Jupiter) – planets and satellites: interiors – planets and satellites: magnetic fields

Online-only material: color figures

1. INTRODUCTION

1.1. Convective Bursts and Saturnian Time Variability

Motions in the convection zones of planets and stars are subject to the dynamical effects of rotation. Feedback and competition between convection and rotation can largely control the patterns of flow heat transfer and magnetic field generation. Intermittent behavior is common in many dynamical systems. The Madden Julian Oscillation may be described as a quasiperiodic spatially localized convection event in Earth's troposphere (Zhang 2005). It is also possible that periodic convective bursts or spatially localized convection can explain the "active longitudes" observed in solar and stellar magnetism (e.g., Berdyugina & Usoskin 2003; Brown et al. 2008).

A dramatic example of periodic bursting occurs on Saturn, where observations of its weather layer have revealed a fascinating time-variable dynamical history. In 1990, a powerful storm called the Great White Spot (GWS) erupted near the equator and, over about a month, filled the equatorial region with bright clouds and visible flow structures. Similar events have been observed to recur with Saturn's orbital period of about 30 Earth years (Sanchez-Lavega et al. 1991). The most recent great storm occurred on Saturn in 2010 December. This storm occurred earlier than expected for a GWS and was centered at 38°N latitude, which is near the northern limb of Saturn's equatorial jet (Fischer et al. 2011; Read 2011; Sanchez-Lavega et al. 2011). More frequent regional storms have also been observed in the equatorial region and at higher latitudes on Saturn (Porco et al. 2005).

In the interval between the *Voyager* missions of 1980 and 1981 and the *Cassini* space mission, Saturn's equatorial jet displayed strong apparent variability. Depending on the data set, the prograde flow velocity, as observed by the *Hubble Space Telescope* in the 1990s and *Cassini* in the 2000s, seems to have been about 20% to 50% lower than that observed by *Voyager* (Sanchez-Lavega et al. 2000, 2003; Porco et al. 2005; Gombosi & Ingersoll 2010). In the same time interval the period of Saturn's kilometric radio (SKR) emissions, which had defined the International Astronomical Union (IAU) rotation rate for Saturn, appeared to increase by 6 minutes, or roughly 1% of the length of the Saturnian day (Porco et al. 2005; Sanchez-Lavega 2005). While a link between the GWS, the equatorial jet variability, and the apparent planetary rotation slowdown has been suggested (Sanchez-Lavega 2005), no causal relationship between these phenomena has been proposed. The observed increase in the SKR period, in addition to various complexities in the magnetic signatures of Saturn, have been observed by *Cassini* and the *Ulysses* spacecraft. These observations have spurred numerous investigations to gain a better understanding of Saturn's rotation rate, as well as the processes that give rise to the SKR signal (e.g., Giampieri et al. 2006; Southwood & Kivelson 2007; Anderson & Schubert 2007; Gurnett et al. 2009). Measures of the planetary rotation rate independent of the SKR signal have been obtained using *Cassini* gravity data. Helled et al. (2009) found that the full range of SKR signals that have been interpreted as plausible planetary rotation rates are allowed by their gravitationally constrained radial density distributions.

1.2. The Depth of Fast Zonal Flow

It has been hypothesized that the surface winds of Jupiter and Saturn are driven by internal heat sources, which give rise

to convection deep within the outer molecular H–He fluid that envelops the metallic interior (e.g., Jones & Kuzanyan 2009; Kaspi et al. 2009; Heimpel et al. 2005; Yano et al. 2003; Busse 1976; cf. Schneider & Liu 2009; Lian & Showman 2008; Showman et al. 2006). Thermal emission out of Jupiter and Saturn, which is roughly double that of incoming solar radiation, appears to provide evidence for the internal origin of the gas giants' magnetic field and zonal winds (Aurnou et al. 2008). The deep convection hypothesis is supported by studies that show that the scaling of equatorial and high-latitude jet widths may be explained by a tangent cylinder (TC, the imaginary axial cylinder of radius where the equatorial jet is truncated). Fast zonal flows exist outside of the TC and more slowly moving flows are found in the TC interior (Heimpel & Aurnou 2007). Using detailed radial conductivity distributions, Liu et al. (2008) estimated the minimum planetary radii to which fast zonal flow can penetrate as 0.96 R_J for Jupiter and 0.86 R_S for Saturn. The liquid metal interior convects as well, maintaining the Giant Planets' substantial magnetic fields. However, the dynamo source region, which is seated in the liquid metal core and likely includes part of the deep molecular envelope, is subject to strong Lorentz forces that effectively brake large-scale zonal flows (Kirk & Stevenson 1987; Heimpel & Gómez Pérez 2011).

A typical deep interior convective fluid velocity that drives the dynamos of the giant planets may be of the same order as that driving the geodynamo in Earth's liquid iron core (Starchenko & Jones 2002). Secular variations of Earth's magnetic field yield mm s^{-1} fluid velocities—five orders of magnitude slower than the winds on Jupiter and Saturn. Slow flow of the deep interior is consistent with dynamo models that typically generate axial dipolar magnetic fields (such as those of Earth, Jupiter, and Saturn) from small Rossby number flows (e.g., Olson & Christensen 2006).

The physics driving convection and magnetic field generation in Jupiter and Saturn is very different from that powering the solar dynamo. The ultimate power source for the Sun's convection zone is nuclear fusion in the core. In contrast, convection in the gas giants is driven primarily by gravitational and thermochemical differentiation processes (Guillot et al. 2004). Another major difference between the solar interior and the interiors of the Jovian planets is that the solar dynamo is seated in the outer convection zone and tachocline, whereas the Jovian dynamos likely reside primarily in their liquid metal hydrogen cores. Despite these differences, a comparison of the dynamical structures of the three bodies shows striking qualitative similarities, suggesting the universal nature of the interaction of rotation and convection. Strong zonal flow, including a prograde equatorial jet, is observed at the surface of each of the three bodies. The Rossby number $\mathrm{Ro} = V/\Omega R$, which scales the surface flow velocity V to the rotation velocity ΩR, for each of the three equatorial jets is roughly $\mathrm{Ro}_\odot = 0.2$, $\mathrm{Ro}_J = 0.008$, and $\mathrm{Ro}_S = 0.04$ for the Sun, Jupiter, and Saturn, respectively. Flow in the solar interior, and especially in the convection zone, is well constrained by helioseismology, which has revealed that the differentially rotating surface zonal flow is underlain by zonal flow structures that roughly conserve angular velocity radially down to the tachocline. The tachocline is a thin shear layer at about 0.7 $R_\odot$ that is thought to effectively truncate the fast, convectively driven zonal flow and separates the convection zone from the radiative interior, which rotates nearly as a rigid body (Jones et al. 2010; Rempel 2005; Schou et al. 1998). Baroclinicity in the tachocline is argued to explain the helioseismological results that yield differential rotation contour lines that fall between axial and radial alignment (e.g., Rempel 2005; Miesch et al. 2006). Axial alignment is a consequence of the Proudman–Taylor theorem, which holds for nearly isentropic, rotating fluid layers with $\mathrm{Ro} < 1$ (Rempel 2005), as likely applies in the molecular envelopes of Jupiter and Saturn (e.g., Jones 2007; Jones & Kuzanyan 2009).

In deep convection models, the widths of the equatorial jets of the Sun, Jupiter, and Saturn are set by the depth to which the zonal flow can penetrate. Below that radius the zonal flow must rapidly decrease in velocity to explain the latitudinal surface wind structure (Brun & Toomre 2002; Heimpel et al. 2005; cf. Kaspi et al. 2009). As mentioned above, the morphology of quasigeostrophic flows is constrained by the Proudman–Taylor theorem, which results in two-dimensional cylindrical flow structures within a three-dimensional spherical shell. Although it was originally derived for an isothermal, Boussinesq (incompressible) fluid, the Proudman–Taylor theorem holds for the azimuthal velocity component in both incompressible and compressible flows (Jones & Kuzanyan 2009; Rempel 2005; cf. Kaspi et al. 2009). This correspondence between rotational constraints on quasigeostrophic incompressible and compressible flows explains why Boussinesq zonal flow models of Jupiter and Saturn result in an azimuthal velocity component that differs little from the results of comparable anelastic models (Jones & Kuzanyan 2009; Heimpel & Aurnou 2007).

Liu et al. (2008) pointed out the difficulty in slowing high-latitude zonal flow at the depths expected by deep convection models. They argued that fast zonal flows may not penetrate depths greater than about 0.86 R_S and 0.96 R_J for Saturn and Jupiter, respectively, since ohmic dissipation generated by deeper flows would exceed the planetary luminosity. We note, however, that the luminosity assertion has been challenged on the grounds that the ohmic dissipation is strongly dependent on the relative morphology of the velocity and magnetic fields (Glatzmaier 2008; Stanley & Glatzmaier 2010). In any case, truncation of the zonal flows at high latitudes is an interesting problem because axial gradients in the azimuthal velocity requires violation of the Proudman–Taylor constraint, even while Coriolis forces are expected to be dominant in the molecular envelope. However, for fluid outside the TC, no such velocity gradients are required. Thus, we restrict most of our discussion and interpretation to the equatorial jet, which is underlain by the volume of fluid outside the TC. In this fluid volume, only weak axial gradients in azimuthal velocity are expected to exist. Thus viscous, inertial, and Lorentz forces determine the primary force balances for the equatorial jet.

Zonal flows in Boussinesq spherical shell rotating convection are driven by Reynolds stresses as well as by meridional circulation (Tilgner & Busse 1997; Brummell et al. 1998; Aurnou et al. 2007). Recent spherical dynamo models using radially variable electrical conductivity confirm that the depth and breadth of equatorial zonal flow are indeed limited near the level where the Lorentz force balances the Reynolds stress (Heimpel & Gómez Pérez 2011). In the rotation-dominated regime (low Rossby number) meridional circulations are small scale and weak. Thus, zonal flow in Jupiter and Saturn is likely to be driven primarily by Reynolds stress, and the resulting differential rotation is resisted by viscous/turbulent drag at shallow depths and by Lorentz forces at greater depth in the liquid metal core and within the deeper regions of the metallic envelope where electrical conductivity is sufficiently high.

1.3. Bursting Mode in Numerical Models

The interaction of convection and rotation has been shown to display a bursting mode in numerical models applied to planets (Aurnou & Olson 2001; Christensen 2001, 2002; Grote & Busse 2001; Busse 2002) and young stars (Ballot et al. 2007). Sayanagi & Showman (2007) used numerical and theoretical models in the relatively shallow weather layer to investigate the possible link between Saturn's jet variability and the 1990 GWS. They found that the GWS has insufficient energy to explain the apparent 50% slowdown of the of the equatorial jet. Our deep convection model results bear much in common with those of Ballot et al. (2007), which also feature quasiperiodic, spatially localized relaxation oscillations. Their model was applied to young stars, employed fixed heat flux boundary conditions, included the effects of material compression (with a 60-fold background density change via the anelastic approximation), and had a thicker shell geometry (with a ratio of inner to outer boundary radii, $r_i/r_o = 0.59$). Their convective Rossby numbers ($0.06 < \mathrm{Ro}_c < 0.29$) are comparable with ours ($\mathrm{Ro}_c = 0.2$). The strong similarity between the time series and the flow morphology of their solutions compared to ours suggests that the periodic burst regime is a robust mode of convection applicable to both Boussinesq and compressible spherical rotating fluid systems.

Like these previous models, our numerical model does not include electromagnetism, and we make the assumption that the deep interior is rigidified by Lorentz forces, which, as discussed above (see Section 1.2), act to limit velocity gradients where the electrical conductivity is substantial. However, our numerical model is the first, as far as we know, to include the effects of rotational coupling between the convecting fluid and the rigid interior. Our model conserves angular momentum for the entire system, which includes the convecting fluid and the rigid, constant density inner sphere. Thus, changes in the angular momentum of the outer fluid are accompanied by oppositely directed changes in the rigid rotation of the interior, mediated by viscous torque in our model. This viscous torque is a proxy for electromechanical torque that exists in planetary interiors (e.g., Deleplace & Cardin 2006). Our results show strong cyclicity in time, with quasiperiodic convective bursts. A rotating convection oscillation cycle initiates with a localized upwelling and grows into a global-scale convection event that drives, through rotational coupling, strong azimuthal (zonal) flows. The zonal flows then shear out the convective flow structures, effectively truncating the convection. Without the convective driving, the zonal flows then decay on a diffusive timescale. The convection re-initiates when the zonal flows become sufficiently weak, starting the next cycle (e.g., Busse 2002).

2. NUMERICAL MODEL

Boussinesq convection in a rotating spherical shell is governed by the following system of non-dimensional equations:

$$E\left(\frac{\partial \mathbf{u}}{\partial t} + \mathbf{u}\cdot\nabla\mathbf{u} - \nabla^2\mathbf{u}\right) = -\nabla p - 2\,\hat{z}\times\mathbf{u} + \frac{\mathrm{Ra}E}{\mathrm{Pr}}\left(\frac{\mathbf{r}T}{r_o}\right), \quad (1)$$

$$\frac{\partial T}{\partial t} + \mathbf{u}\cdot\nabla T = \left(\frac{1}{\mathrm{Pr}}\right)\nabla^2 T, \quad (2)$$

$$\nabla\cdot\mathbf{u} = 0, \quad (3)$$

where $\mathbf{u}$ is the velocity vector, T is the temperature, and p is the non-hydrostatic pressure. The equations are non-dimensionalized using the spherical shell thickness $D = r_o - r_i$ for length scale, the viscous diffusion time $t = D^2/\nu$ for timescale, ν/D for velocity scale, $\rho\Omega^2 D^2$ for pressure scale, and ΔT for temperature scale. The inner and outer fluid shell boundaries are r_i and r_o, respectively; ν is the working fluid's kinematic viscosity; the initial angular rotation velocity of the system is Ω; and ΔT is the imposed temperature difference across the shell. The inner sphere, $r < r_i$ is solid and has the same density ρ as that of the Boussinesq fluid in the convecting shell.

Equations (1)–(3) describe conservation of momentum, conservation of energy, and fluid continuity, respectively. The non-dimensional control parameters are the following. The Ekman number $E = \nu/(\Omega D^2)$ is the ratio of viscous and Coriolis forces. The Rayleigh number $\mathrm{Ra} = \alpha g_o \Delta T D^3/(\kappa\nu)$ scales the strength of buoyancy forces in the flow, where α is thermal expansivity, g_o is gravity on the outer boundary, and κ is thermal diffusivity. The Prandtl number $\mathrm{Pr} = \nu/\kappa$ is the ratio of viscous and thermal diffusivities. Lastly, the radius ratio $\chi = r_i/r_o$ defines the spherical shell geometry, where r_i and r_o are the inner and outer boundary radii. The model outputs discussed are the Reynolds and Rossby numbers. The Reynolds number $\mathrm{Re} = UD/\nu$ is the scaled ratio of inertial and viscous forces, where U is a characteristic output velocity. The Rossby number $\mathrm{Ro} = U/(\Omega r_o) = \mathrm{Re}E(1-\chi)$ is the scaled ratio of inertial and Coriolis forces. We use the outer radius as the length scale in our model output Rossby number for convenient comparison to planetary Rossby numbers.

The equations of motion (1)–(3) are solved simultaneously via the numerical code MAGIC (Wicht 2002; Christensen & Wicht 2007). This pseudo-spectral code, which is based on the original legacy code of Glatzmaier (1984), uses mixed implicit/explicit time stepping and has been benchmarked (Christensen et al. 1999). Values of control parameters for the simulation shown are $E = 10^{-5}$, $\mathrm{Ra} = 4\times10^7$, $\mathrm{Pr} = 0.1$, and $\chi = 0.85$. In the full-sphere calculation presented here, the resulting time-averaged Rossby number in the equatorial jet is roughly $\mathrm{Ro} = 0.01$, which corresponds to $\mathrm{Re} = 6.7\times10^3$. The thermal boundary conditions are fixed temperature. The velocity boundary conditions on r_o are mechanically impenetrable and stress free, whereas the velocity conditions on r_i are impenetrable and non-slip. The rigid inner sphere is free to rotate about the axis of the rotating frame of the outer sphere working fluid. Changes in the angular momentum of the inner sphere are given by $I\,\partial\omega_i/\partial t = \Gamma$, where ω_i is the inner sphere rotation rate, I is its moment of inertia (MOI), and Γ is the viscous torque. Details of the numerical implementation of the lower boundary condition and inner sphere rotation can be found in Wicht (2002) and Hollerbach (2000). The initial conditions are zero motion relative to the rotating frame and a random thermal perturbation, from which convection develops. The model was run for over 4500 planetary rotations, corresponding to 0.28 viscous diffusion times. Solving the governing equations on a full sphere, we use 384 points in latitude $l_{\max} = 256$, 768 points in longitude, and 49 points in radius. Convergence of the numerical simulation required the use of a hyperdiffusion scheme:

$$d(l) = d_o\left(1 + A\left[\frac{(l+1) - l_{\mathrm{hd}}}{(l_{\max}+1) - l_{\mathrm{hd}}}\right]^{\beta}\right). \quad (4)$$

Here $d(l)$ is the diffusivity that varies as a function of spherical harmonic degree l, d_o is the non-hyperdiffusive diffusion ampli-

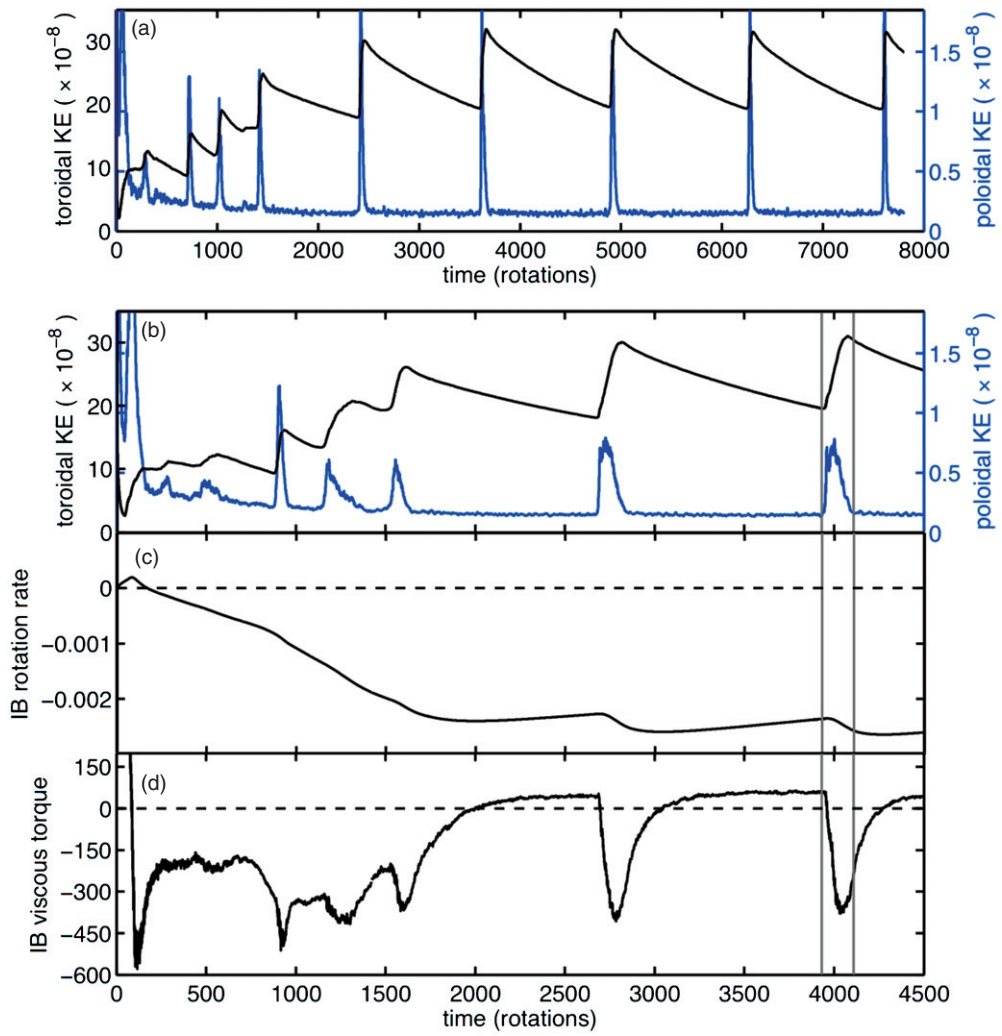

Figure 1. Time series for two numerical runs. Figure 1(a) shows the poloidal and toroidal kinetic energy for a case run in a quarter section of a sphere. Other than the four-fold symmetry, the quarter-section case is identical to the full sphere calculation (b)–(d), which is the focus of this paper. Vertical gray lines in (b)–(d) represent time snapshots referred to subsequent figures. Note that in (a) and (b) the toroidal kinetic energy scale (vertical axis) is greater than the poloidal energy scale by a factor of 20.

(A color version of this figure is available in the online journal.)

tude, the hyperdiffusion amplitude is A, the spherical harmonic degree at which the hyperdiffusion starts to act is $l_{\rm hd}$, and β is the hyperdiffusion exponent. We have set $A = 300$, $l_{\rm hd} = 5$, and $\beta = 2$ in the present calculations. Based on tests at higher Ekman comparing runs with and without hyperdiffusion, we find that the level of hyperdiffusion used here does not qualitatively alter the results.

In our numerical model, the liquid metal interior is treated as a rigid inner sphere that may rotate relative to the overlying fluid. The inner sphere's direction of relative rotation is governed by viscous torques. Thus, angular momentum may be exchanged between the working fluid and the interior, while the total angular momentum is conserved.

2.1. Modeling Results

Figure 1 shows time series from a numerical simulation in a full sphere. After a spin-up period of roughly 2500 rotations (0.16 viscous diffusion timescales) two powerful convective bursts occur at around 2700 and 4000 rotations (Figure 1(b)). Figure 2 shows the time series for the single convective burst that peaks at about 4000 rotations. The subsequent figures also describe aspects of that event, which we refer to as the "burst" or "storm." In Figure 1(b), it is not obvious that the system achieves a statistically steady state. Therefore, we have also performed less computationally expensive models that employ the same parameter values, but integrated over longer timescales using lower resolution and spherical sections with azimuthal symmetry. Such a calculation, shown in Figure 1(a), indicates that the last two bursts in the main simulation presented here are the first two of a longer series of periodic bursts for longer calculation times. The periodic bursts are characterized by a 10-fold increase in the poloidal kinetic energy, which precede a roughly 1.5-fold increase in the toroidal kinetic energy. Here, the poloidal energy is a measure of strength of convection, while the toroidal energy scales the strength of zonal flow. The total poloidal and toroidal kinetic energies in the rotating frame are plotted. The toroidal energy is dominated by the axisymmetric component (i.e., the zonal flow), whereas the nonaxisymmetric toroidal energy is less than 1% of the total toroidal energy. The time series clearly show that convective bursts periodically drive the zonal flow (top plots of Figures 1 and 2). Since the system conserves angular momentum, the interior rigid sphere undergoes retrograde acceleration as the equatorial jet spins up in the prograde direction (middle plots of Figures 1 and 2).

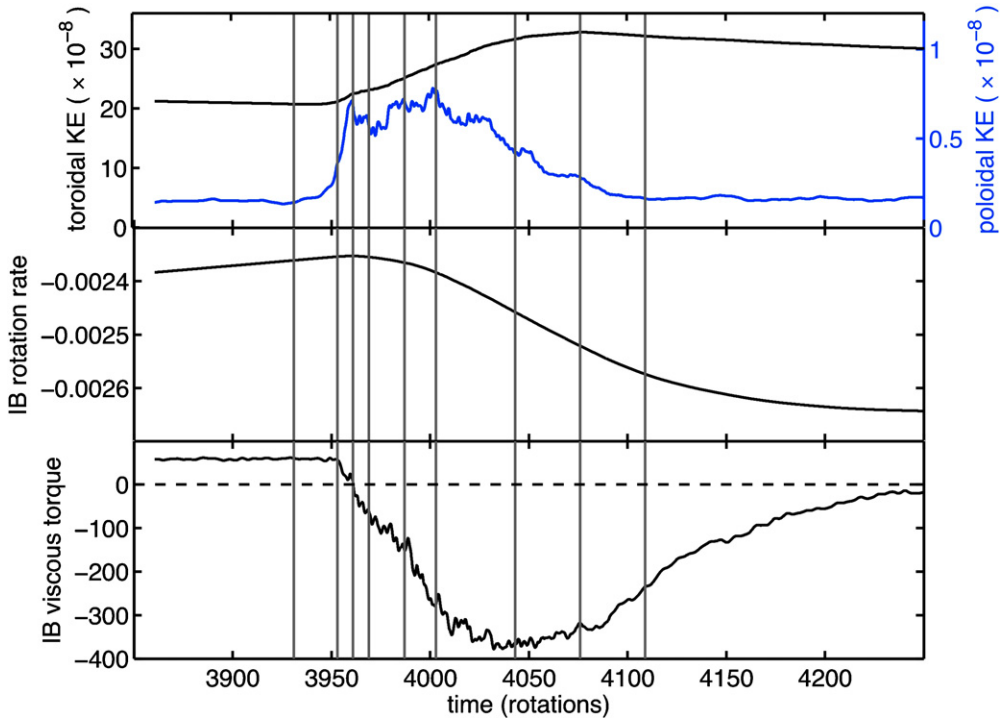

Figure 2. Time series of a convective burst. Gray vertical lines show the times corresponding to the images in Figure 4.
(A color version of this figure is available in the online journal.)

The transfer of angular momentum between the fluid layer and the inner sphere is mediated by a retrograde viscous torque at the inner boundary (bottom plots of Figures 1 and 2).

Figure 3 shows the azimuthally averaged viscous torque near the inner sphere boundary (bottom of the numerical model fluid layer) as a function of time and latitude for the convective burst that peaks near 4000 rotations. The time range of the figure is similar to that of Figure 2. It is seen that bands of prograde and retrograde torque at mid-latitudes are only weakly affected by the burst. Greater variability occurs near the equator. Before the burst an equatorial band of prograde torque is responsible for the overall weakly prograde torque seen in Figures 1 and 2. During the convective burst the band of prograde torque vanishes due to the strengthening and expansion of low-latitude bands of retrograde torque north and south of the equator. As the burst subsides the band of prograde torque reestablishes itself at the equator.

Convection during the burst is visualized in Figure 4. Each of the nine pairs of images show the temperature field on a spherical surface just beneath the outer boundary. This is circumscribed by the corresponding temperature field in the equatorial plane. The prograde rotation direction is from left to right for the inner image and counterclockwise for the surrounding equatorial slice. At $t = 3931$ rotations the system is relatively quiescent between convective bursts and heat flow is lower in the equatorial regions than at higher latitudes. This heat flow pattern is characteristic of quasigeostrophic rotating convection in spherical shells with free slip boundary conditions (e.g., Aurnou et al. 2008). Heat flow is suppressed outside the TC (at low latitudes) by the equatorial jet. Strong shear, associated with the jet inhibits the ascent of convective plumes in cylindrical radius. However, since convection drives the equatorial jet, the period between convective bursts is one of decreasing equatorial jet velocity. Near the end of a cycle, the decreased jet velocity allows for the emergence of a new convective burst, which can be seen as a thermal disturbance at $t = 3953$. The burst develops by azimuthal propagation of the area of upwelling and by advection of the heated fluid. The fine structure of upwelling can be seen as columnar plumes that are narrow in longitude but are elongated in the axial direction and fill the region exterior to the so-called TC (e.g., see Figure 2 in Heimpel & Aurnou 2007). During the burst, plume propagation proceeds mostly in the prograde direction. In addition, advection associated with the background flow in the equatorial jet carries the warm fluid prograde, so that the whole plume structure drifts in the prograde direction. The background prograde zonal flow may aid in the development of the storm. As the zonal flow advects rising plumes downstream of the developing storm, the displaced unstable flow may initiate further plume activity. This would explain the directional coherence of prograde advection and propagation. Since plume activity in the region of the sphere where the storm initiated ceases before the event ends, the thermal disturbance does not fill the entire TC at any snapshot in time. However, since the entire storm is advected in a prograde sense, the storm eventually encircles the globe in the region outside the TC. (To see this, compare, in Figure 4, $t = 3953$ and $t = 4043$ rotations, noting that the prograde direction is counterclockwise for the equatorial slices.)

Figure 5 shows snapshots of azimuthal velocity V_ϕ (left column) and latitudinal velocity V_θ (right column), relative to and near the inner boundary before, during, and after a burst event, in Mollweide projection. The relative velocity V_ϕ is a measure of the viscous shear stress that generates prograde and retrograde torques on the rigid inner spherical boundary. The sequence of images may be compared to the bottom plot of Figure 2, which shows the viscous torque, integrated globally over the inner boundary. At time $t = 3931$ rotations, lightly prograde equatorial flow (and prograde viscous torque) precedes the burst event. This prograde flow is accompanied by latitudinally divergent boundary flow at the equator (see the

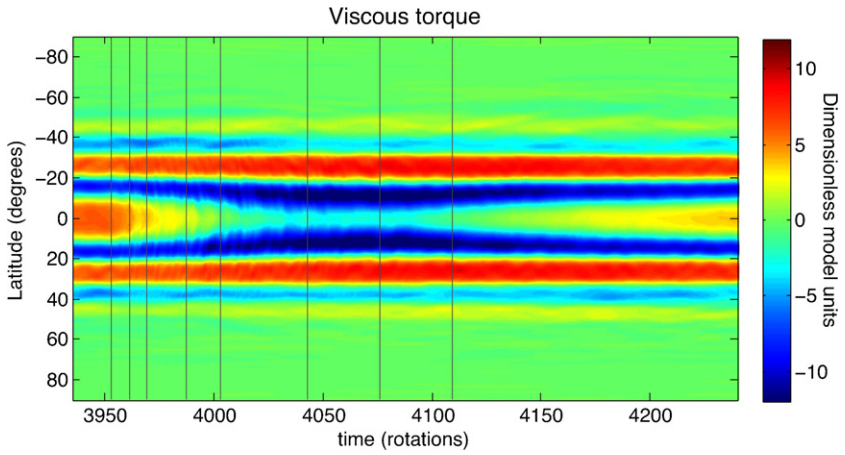

Figure 3. Viscous torque, as a function of time and latitude, for a convective burst. Gray vertical lines show, as in Figure 2, times corresponding to the images in Figure 4.

(A color version of this figure is available in the online journal.)

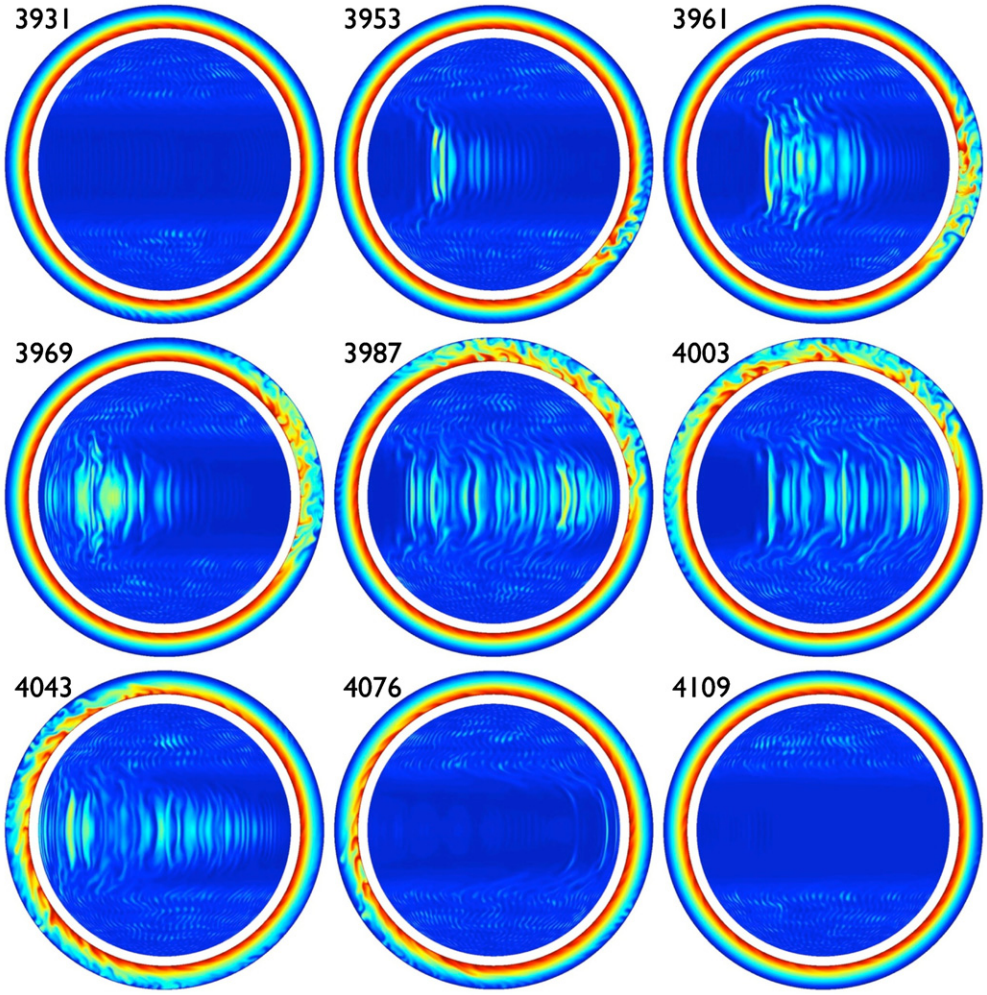

Figure 4. Snapshots of temperature at times (rotation units) shown in the upper left and corresponding to the vertical lines in Figure 2. Outer images show the temperature in an equatorial slice over the entire depth (outer boundary R and inner boundary $0.85R$). Inner images are orthographic projections of the temperature near the outer surface (at $0.99R$). Storm activity develops as a localized disturbance of plumes and high near-surface temperatures. The storm broadens and propagates in the prograde direction. The equatorial slice images are all shown in the same rotating reference frame position, while the middle and bottom rows of near-outer-surface images are shifted to show the storm development (middle row shifted by 60 degrees longitude and bottom row by 140 degrees with respect to the top row).

(A color version of this figure is available in the online journal.)

caption of Figure 5 for relation between color and flow direction). During the burst event, shown at $t = 3987$ rotations, strong and localized viscous stress in prograde and retrograde, and in the poleward and equatorward directions develop with turbulent convection. However, as the storm recedes, the flow again becomes more organized, but with directions

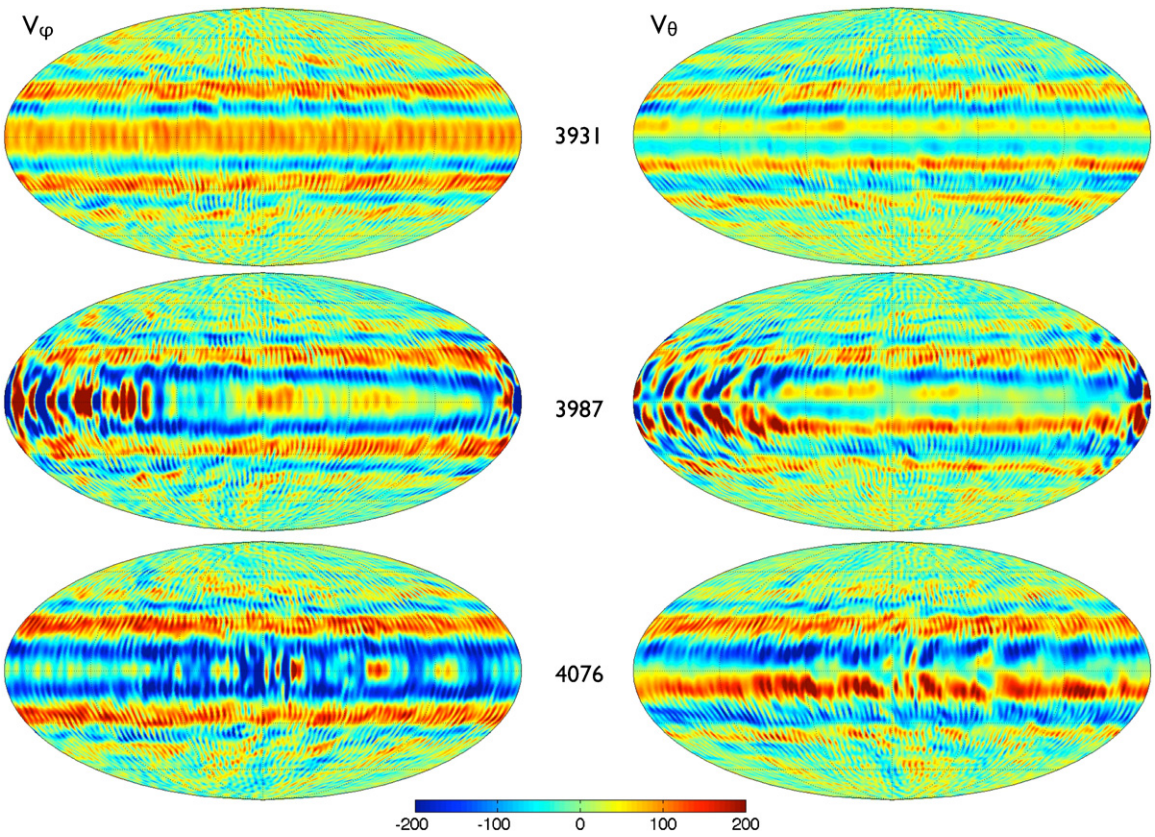

Figure 5. Mollweide projections of the horizontal velocity field relative to and near the inner boundary ($r/r_o = 0.8502$, where $r_i/r_o = 0.85$). This differential velocity is a measure of the viscous stress on the inner boundary. Color bar shows model velocity units. Prograde and retrograde V_ϕ are red and blue, respectively. For V_θ poleward and equatorward flows are red and blue, respectively, in the northern hemisphere. The numbers between the two columns of images give the time (in number of rotations) of each snapshot.

(A color version of this figure is available in the online journal.)

reversed, as is evident immediately after the storm, at $t = 4076$ rotations.

The azimuthal velocity and meridional flow at a longitude slice is shown for five snapshots in Figure 6. The meridional flow is axially elongated and of small scale in the direction perpendicular to the rotation axis relative to the layer depth. The latitudinally confined meridional flow structure is characteristic of a rotationally dominated (low Ro) three-dimensional flow (e.g., Liu & Schneider 2010). At an early stage of the convective burst, the pair of images at $t = 3965$ shows an increase in the magnitude but not the pattern of meridional flow near the inner boundary, while near the outer boundary a decrease in the azimuthal velocity corresponds to greatly increased small-scale meridional flow. Later, a reorganization and reversal of meridional flow near the inner sphere boundary of the numerical model is accompanied by the development of a band of strongly retrograde azimuthal flow (see $t = 3987$ and $t = 4043$ and compare with Figures 3 and 5).

Figure 7 shows profiles of temperature and velocity (scaled as Ro) during an early stage of a convective burst and immediately after the event. The profiles after the storm (at time $t = 4076$ rotations) are averaged over all ϕ. The profiles during the burst are averaged azimuthally over the active region of the storm and over the region antipodal to the storm region. Thus, although both storm and antipodal regions represent the same snapshot in time ($t = 3961$ rotations), the antipodal profiles show the state of the system immediately preceding the local arrival of the storm. The T-axes in Figures 7(a) and (b) show the full temperature range between the inner and outer boundaries. Thus, Figure 7(a) shows that the early-storm temperature fluctuation is strong and regionally constrained. The radial temperature profile is nearly conductive before the local arrival of the storm, as indicated in Figure 7(b). In contrast, strong convection in the storm region results in the development of thermal boundary layers and a steeper, thermal profile indicating a strongly mixed fluid interior. The post-storm profile in Figure 7(c) shows that the convective burst results in a stronger equatorial jet. However, near the start of the storm, the peak equatorial jet velocity near the outer boundary actually decreases. At the start of the burst, fluid is advected from near the bottom boundary toward the top. This overturn of the fluid layer causes the azimuthal velocity in the outer part of the spherical shell to decrease. This can be seen in Figure 7(c): in the storm region the prograde velocity is decreased, relative to the antipode region, outside roughly $r = 0.91$, with a strong velocity reduction at the outer boundary. However, the nonaxisymmetric convective plumes that constitute the storm region generate net azimuthal Reynolds stresses that act over time to accelerate the equatorial jet to higher velocity. Subsequently, during the relaxation phase between convective bursts, the jet slows gradually before commencing a new cycle (see also Figure 1).

As the storm wanes and ceases, retrograde torque on the interior boundary decays toward zero, which is achieved roughly 300 rotations after commencement of the convective burst. This is followed by a longer period (of about 1000 rotations) where the interior boundary experiences a weak prograde torque,

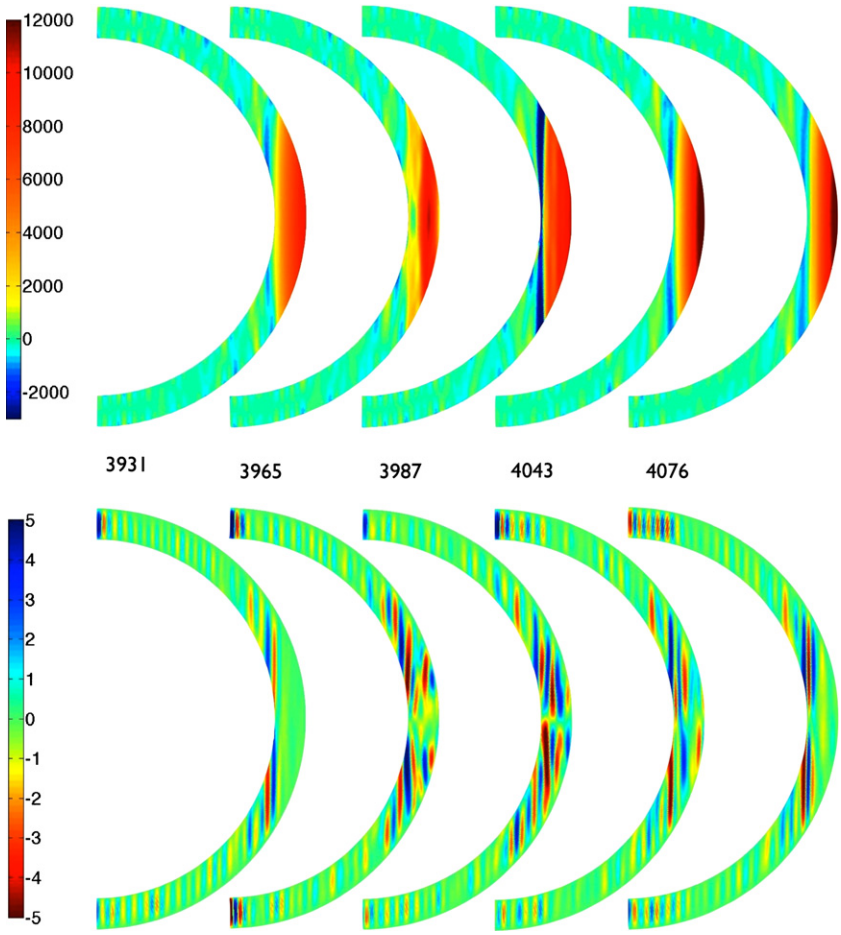

Figure 6. Meridional slices of the azimuthal fluid velocity V_ϕ relative to inner boundary velocity (top row), and the axisymmetric stream function (bottom row). Each pair of images is a snapshot in time, indicated by the rotation number. For the top row, the color bar is scaled by the Reynolds number. Red and blue indicate prograde and retrograde flows, respectively. For the bottom row, red and blue indicate clockwise and counterclockwise flows, respectively. The longitude for each snapshot corresponds to the extreme (right or left) edge of the Mollweide projections shown in Figure 5.

(A color version of this figure is available in the online journal.)

associated with the viscous decay of the equatorial jet flow. A new cycle begins with another convective plume event. The period of a burst cycle is roughly 1300 rotations. The change in rotation rate of the interior from 3960 rotations to 4300 rotations represents 0.034% of the system's initial rotation rate, Ω.

In our models, a convective burst event corresponds to the rapid development of a propagating cluster of convective plumes near the equator. The plumes overcome strong rotational forces that tend to stabilize convection, and advect warm fluid from the inner boundary radially toward the outer boundary. We find that during the early stage of a storm the rotation of the inner sphere remains roughly steady (see Figure 2), which means that, early on, angular momentum of the working fluid is approximately conserved. Thus, the Coriolis force acting on radially ascending fluid causes the outer part of the equatorial jet to slow down, and a dimple of anomalously low azimuthal surface velocity develops in the equatorial region (see Figures 6 and 7(c)). We can also understand the decreased surface velocity as the result of radial mixing of angular momentum. The short timescale effect of the burst event is to decrease the radial velocity gradient in the working fluid (see Figure 7(d)) as angular momentum in the working fluid is approximately conserved. However, the influx of radial momentum from the convective burst is then spun up in the prograde azimuthal direction by Reynolds stress, in a process that leads to a subsequent net increase in the angular momentum of the working fluid. The development of small-scale meridional circulation and the subsequent, longer timescale increase in the zonal flow velocity shown in Figure 6 illustrates this process. Since angular momentum is conserved in the entire system, the inner sphere rotation rate slows as the working fluid layer accelerates in the prograde direction. This adjustment is mediated in our model by viscous torque. Fluid that rises in convective plumes, away from the inner boundary, is replaced by equatorward flow near the inner boundary. Like the outward flowing plume, equatorward flow along the spherical boundary travels away from the rotation axis and curls in the retrograde direction. Hence this boundary layer flow generates strong retrograde viscous torque on the interior boundary, slowing down the rotation rate of the interior (see Figures 1, 2, 3, 5, and 6).

3. SCALING OF ANGULAR MOMENTUM EXCHANGE

3.1. Giant Planet Spin-up Timescales

It can be seen in Figures 1 and 2 that the changes in inner boundary torque and rotation rate lag the poloidal kinetic (i.e., convective) energy. The peak retrograde torque occurs about 30 rotations after the peak poloidal energy. This phase lag gives an idea of the timescale required, in our model, for Reynolds stress

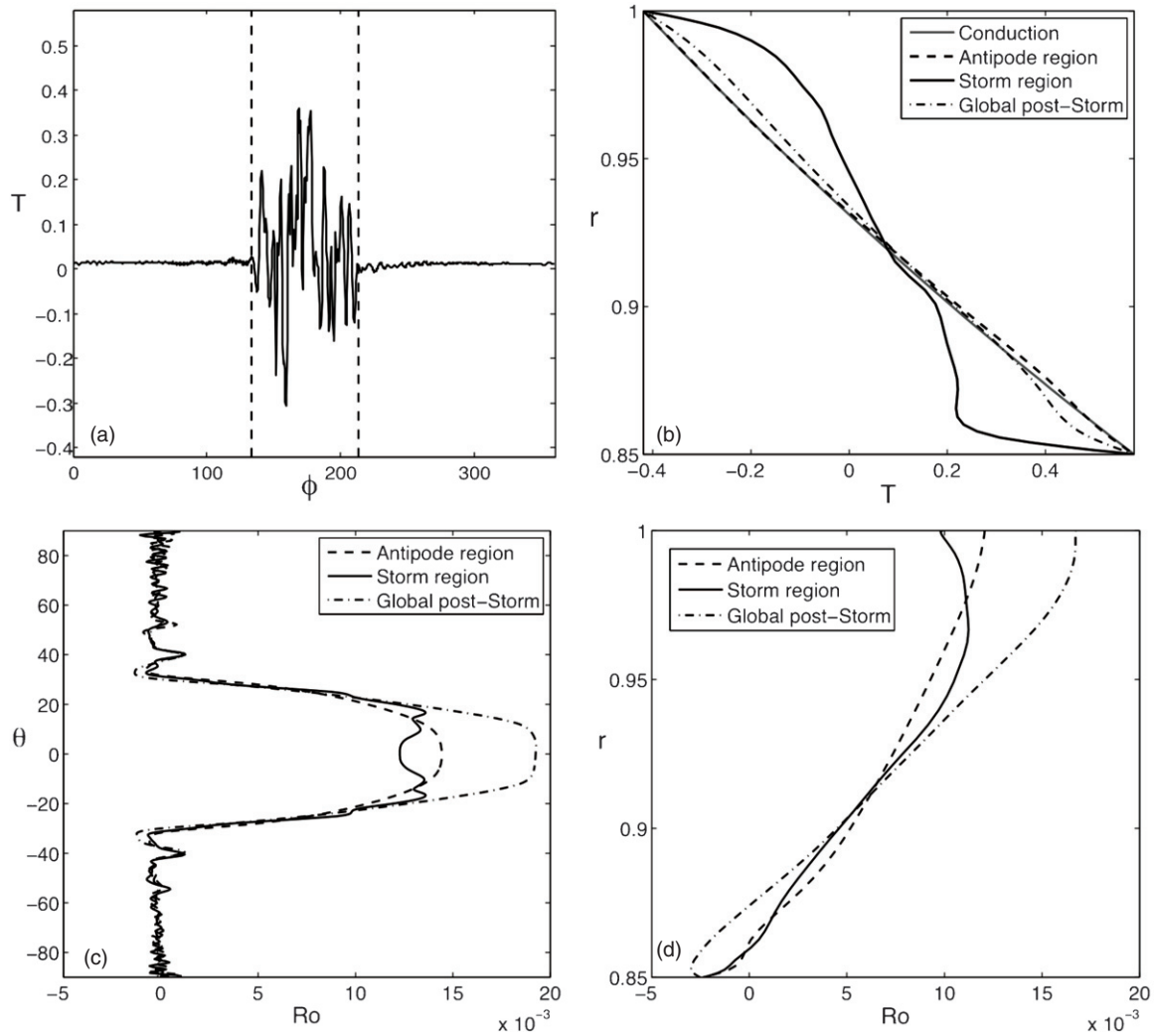

Figure 7. Temperature (T) and azimuthal velocity (Ro $= V_\phi/\Omega R$) profiles during and after a convective burst. The equatorial temperature at an early stage of a convective burst ($t = 3961$ rotations) is plotted in (a). The dashed lines define the storm region indicated in (b)–(d). The antipode region has the same ϕ-width as the storm region. For $t = 3961$ rotations T and Ro are averaged in ϕ over the storm and antipode regions. Global post-storm refers to $t = 4076$ rotations, immediately after the convective burst. For these profiles T and Ro are averaged over all ϕ. The equatorial temperatures are plotted as a function of depth in (b). The velocities at the surface, relative to the bottom boundary velocity are plotted in (c). The equatorial velocities are plotted as a function of depth in (d).

to spin up the convective momentum released by the storm. For reference, Saturn's IAU standard System III rotation period is 10 hr 39 minutes 24 s (Porco et al. 2005). We may compare our numerical result to the characteristic spin-up timescale:

$$\tau_E = \left(\frac{L^2}{\nu\,\Omega}\right)^{\frac{1}{2}} = \frac{1}{\Omega}\left(\frac{1}{E}\right)^{\frac{1}{2}} \tag{5}$$

(Greenspan & Howard 1963). For our numerical model, with $L = D$ being the spherical shell depth, rotation period T, and $E = 10^{-5}$, we find that $\tau_E \simeq T/(2\pi\sqrt{E}) \simeq 50$ rotations. Since planetary fluids have much lower molecular (and even turbulent) values of viscosity than current numerical models, their characteristic spin-up times are much longer. The radial kinematic viscosity structure in the molecular envelopes of the giant planets is not well known. Guillot et al. (2004) gives an estimate for the Ekman number of Jupiter ($E \sim 10^{-15}$) that is similar to estimates for the Earth's core (e.g., Jones 2007). That estimate, based on a molecular viscosity, gives a spin-up time of several thousand years. Much shorter spin-up timescales result from estimates using turbulent diffusion coefficients. Starchenko & Jones (2002) use mixing length theory to obtain $\sim 10^3$ m^2 s^{-1} as an estimate of the three turbulent diffusion coefficients (viscous ν_*, thermal κ_*, and magnetic λ_*) for Jupiter and Saturn. That estimate, with a Saturnian fluid layer depth $D \sim 5 \times 10^7$ m and rotation rate $\Omega = 1.64 \times 10^{-4}$ s^{-1}, yields $E \sim 2 \times 10^{-9}$ and a spin-up time of about 3600 Saturn rotations (4 Earth years). Following the approach of Jones (2007), we can make an intermediate estimate by taking the turbulent viscosity to be similar to a planetary value of the metallic hydrogen magnetic diffusivity ($\lambda \sim 4$ m^2 s^{-1}; Nellis et al. 1996), which is the greatest of the three primary material diffusivities in the deep interiors of the giant planets. Thus, assuming $\nu_* \sim \kappa_* \sim \lambda$ gives $E \sim 10^{-11}$ and a Saturnian spin-up time of about 60 Earth years.

To estimate the spin-up timescale of the deep interior in response to angular momentum changes in the molecular envelope, we must take into account the timescale over which rigidity can be imposed by the interior magnetic field. However, electromagnetic spin-up away from solid boundaries has not been studied in detail (cf. Benton & Loper 1969; Loper & Benton 1970). Furthermore, any such electromagnetic spin-up

estimates are fraught with uncertainty for Jupiter and Saturn because of strong and poorly constrained gradients in the electrical conductivity associated with the transition from the molecular envelope to the liquid metal core. The nature of that transition is an area of active research, as is the equation of state for hydrogen. Nellis et al. (1996) used shock experiments to estimate a hydrogen metallization pressure of 140 GPa, which corresponds to 0.9 R_J in Jupiter, and to 0.63 R_S in Saturn (Liu et al. 2008; Helled et al. 2009). We will refer to radial conductivity profiles for Jupiter and Saturn of Liu et al. (2008). Those profiles were constructed using the conductivity data of Nellis et al. (1996, 1999) and equations of state of Guillot (1999). The major uncertainties in the electrical conductivity of the interiors of giant planets comes from uncertainties in the distribution of H_2 and monatomic H, the distribution of helium, and the effect of elements in minor abundances such as O and the alkali metals (Nellis et al. 1999; Liu et al. 2008; Nettelmann et al. 2008). In particular, Saturn has an He-depleted atmosphere (relative to cosmic, solar, and Jovian abundances). Assuming the planetary abundance of helium is not anomalous, this implies an increase of He with depth. However, interior models differ as to the present radial He distribution. The miscibility of hydrogen and helium, and the existence and dynamics of a "helium rain" layer might possibly also be important in giant planets (Salpeter 1973). Such a layer, which may affect the dynamics of the transition from the core to the outer molecular envelope, has been studied in relation to the origin of Saturn's highly axisymmetric magnetic field (Stevenson 1982; Stanley & Mohammadi 2008).

The appropriate form of the spin-up time depends on the balance of dominant forces in the interior. While buoyancy is an important force in the dynamics of convection and magnetic field generation, we neglect it for this discussion because it acts radially, and we are mainly interested in horizontal motions (cf. Brito et al. 2004). We are then left with the viscous, inertial, Lorentz, and Coriolis forces. We can choose to scale these forces by the Ekman, Elsasser, and Alfvén numbers. The Elsasser number

$$\Lambda = \frac{B^2}{\rho\mu\lambda\Omega} \tag{6}$$

is the ratio of the Lorentz to Coriolis forces. The magnetic permeability μ is taken to be that of free space (planetary interior temperatures are far above the Curie point). The Alfvén number

$$A = \frac{V_A}{V} = \left(\frac{B^2}{\rho\mu V^2}\right)^{1/2} \tag{7}$$

represents the balance between Lorentz and inertial forces, and is estimated as the ratio of the Alfvén wave speed and flow velocity.

The torsional Alfvén wave is particularly attractive as the basis for a deep interior spin-up time since it acts to straighten torsionally distorted magnetic field lines. Indeed, Alfvén waves have been studied as a primary source of torsional oscillations, which are thought to be the origin of Earth's decadal scale length of day variations (Gillet et al. 2010; Braginsky 1970). For Saturn, we can consider a great storm as providing a large-scale azimuthal velocity perturbation that can bend poloidal magnetic field lines at depths where the electrical conductivity is sufficient. Spin-up then proceeds as an Alfvén wave that propagates downward. The characteristic magnetic spin-up timescale is the crossing time of an Alfvén wave of velocity V_A over the length scale of interest L:

$$\tau_A = L/V_A = \left(\frac{L^2\rho\,\mu}{B^2}\right)^{\frac{1}{2}} = \tau_E\left(\frac{\mathrm{Pm}}{\Lambda}\right)^{\frac{1}{2}}, \tag{8}$$

where $\mathrm{Pm} = \nu/\lambda$ is the magnetic Prandtl number. The Alfvén spin-up timescale does not depend on any diffusion coefficients, which have been argued to be either poorly constrained or weakly relevant in planetary dynamos (Christensen & Aubert 2006; Olson & Christensen 2006). Comparing Equation (5) with Equation (8) it is evident that $\tau_A \ll \tau_E$ in the dynamo source region, where $\mathrm{Pm} \sim 10^{-5}$ and both A and Λ are likely larger than 1, perhaps of order 10 or greater. Thus τ_A is expected to be the dominant spin-up time in the deep interior.

The intensities of the surface magnetic fields of Jupiter and Saturn have been stable at about 4.2×10^{-4} T and 2.1×10^{-5} T, respectively, over the past four decades of spacecraft observations (Russell & Dougherty 2010). These values correspond to Elsasser numbers $\Lambda \sim 0.2$ for Jupiter and $\Lambda \sim 5 \times 10^{-4}$ for Saturn, based on $\rho = 1000$ kg m^{-3} and $\lambda = 4$ m^2 s^{-1}, values representative of the giant planets' liquid metal cores. In the deep interior, magnetic fields are much higher, and a magnetostrophic balance (i.e., Elsasser number Λ of order 1) is typically assumed for planetary dynamos (e.g., Stevenson 2003). However, the Lorentz force may be regionally stronger than the Coriolis force within the dynamo source region. Numerical models typically have Elsasser numbers $0.1 \lesssim \Lambda \lesssim 10$ at the top of the core, but higher values, often by factors of 10 or 100, in the source region (e.g., Glatzmaier 2002; Rotvig & Jones 2002).

To estimate the interior magnetic field we must take into account amplification of the dynamo-generated field by regional fluid motions. Amplification of the toroidal component of the magnetic field occurs by differential rotation via the ω-effect. The high-speed azimuthal flow in the semi-conducting molecular envelope can act upon the poloidal magnetic field B_p to generate a toroidal field that scales as

$$B_\phi \sim \mathrm{Rm} B_p \tag{9}$$

(e.g., Roberts 2007), where the magnetic Reynolds number

$$\mathrm{Rm} = \frac{V L_\lambda}{\lambda} \tag{10}$$

is defined in terms of the magnetic diffusivity λ and its scale height L_λ. Magnetic induction overtakes magnetic diffusion when $\mathrm{Rm} > 1$. Taking $V \sim 100$ m s^{-1} as the velocity scale for Saturn, the diffusivity profiles of Liu et al. (2008) yield $\mathrm{Rm} \sim 1$ at a radius of $\sim 0.88\ R_S$, where $\lambda \sim 2 \times 10^7$ m^2 s^{-1} and $L_\lambda \sim 2 \times 10^5$ m. Similarly, for Jupiter, $\mathrm{Rm} \sim 1$ at $\sim 0.96\ R_J$.

We refer to the transition between fast zonal flow and the deeper magnetically controlled interior as the planetary tachocline, which may play a similar role to the solar tachocline in that it represents a relatively thin layer with a strong velocity gradient that separates the differentially rotating exterior from the more or less rigidly rotating interior (see Figure 8). Planetary tachoclines are expected to develop well within the molecular envelopes of Jupiter and Saturn because of the steep radial electrical conductivity gradient. Fast zonal flow at radial levels where the electrical conductivity is high results in high Rm, which in turn results in strong magnetic torques to counter the flow. Thus, the flow velocity and magnetic induction must saturate.

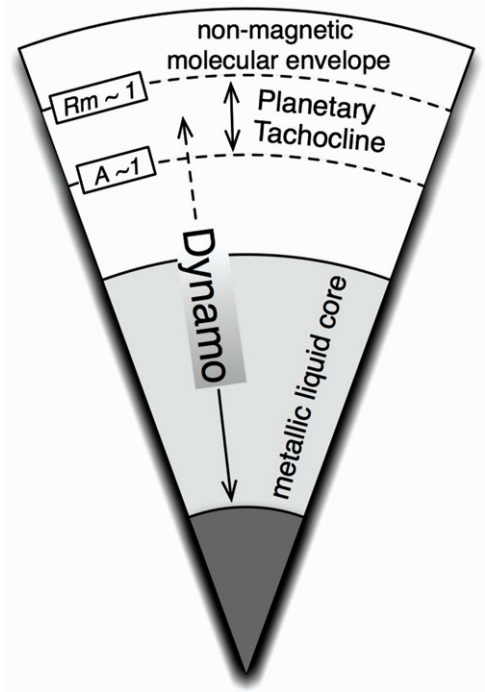

Figure 8. Schematic illustration of interior dynamical features of Saturn as discussed in the text. The radius where Rm = 1 is estimated to be $r \sim 0.88\ R_S$. The radius where $A = 1$ is estimated to be $r \sim 0.78\ R_S$.

There is a tradeoff between the velocity field versus density and magnetic diffusivity in the molecular envelopes of the giant planets. The increasing density and decreasing magnetic diffusivity with depth both tend to slow the zonal flow velocity. The locally generated magnetic field is expected to increase with depth as the diffusivity approaches the metallic hydrogen value of $\sim 4\ \mathrm{m^2\ s^{-1}}$ (e.g., Nellis et al. 1996). However, the magnetic field will saturate as the flow velocity saturates due to increasing Lorentz forces. The classical saturation limit is reached when the kinetic and magnetic energy densities achieve equipartition, which corresponds to $A \sim 1$ (e.g., Galloway et al. 1977). However, interior magnetic fields of stars and planets are thought to exceed the equipartition limit (e.g., Galloway et al. 1977; Gómez-Pérez & Heimpel 2007; Christensen et al. 2009). Still, the depths between the radii where Rm = 1 and $A = 1$ approximate the transition between velocity-dominated and magnetic-field-dominated interior dynamics. We can therefore regard this radius range as representing the thickness of the planetary tachocline.

Estimates of the radius where $A \sim 1$ can be obtained by combining Equations (7), (9) and (10), such that

$$A \sim \frac{B_0^2 L^2}{\rho\, \mu\, \lambda^2}. \qquad (11)$$

For Saturn, with the poloidal field component estimated by downward continuation of the external field to be $B_0 \sim 4.4 \times 10^{-5}$ T, and with $V \sim 2 \times 10^{-3}\ \mathrm{m\ s^{-1}}$ (Starchenko & Jones 2002), $\rho \simeq 530\ \mathrm{kg\ m^{-3}}$ (Helled et al. 2009), $\lambda \sim 2 \times 10^3\ \mathrm{m^2\ s^{-1}}$, and $L_\lambda = 10^6$ m (Liu 2006), we can estimate that $A = 1$ at $\sim 0.78\ R_S$. Similarly, for Jupiter, $B_0 \sim 5.2 \times 10^{-4}$ T, $V \sim 10^{-3}\ \mathrm{m\ s^{-1}}$ (Starchenko & Jones 2002), $\rho \simeq 380\ \mathrm{kg\ m^{-3}}$ (Nettelmann et al. 2008), $\lambda \sim 10^4\ \mathrm{m^2\ s^{-1}}$, $L_\lambda = 5 \times 10^5$ m (Liu 2006), and $A = 1$ at $\sim 0.93\ R_J$. A schematic cross section of what Saturn's dynamical structure may look like, based on these estimates, is shown in Figure 7.

3.2. Moment of Inertia of Saturn's Equatorial Jet

We have estimated that the timescales for changes in angular momentum for Saturn's deep interior are much shorter than the spin-up time for the shallower, nonmagnetic molecular envelope, and likely less than the period between the *Voyager* and *Cassini* missions. In order to estimate the amplitude of angular momentum transfer from the zonal flow region to the deep magnetically "rigid" interior we can calculate the relative MOI of the volume of fluid mobilized by a convective burst. For a uniform density sphere, which is the case of our numerical model, with radius ratio $\chi = 0.85$, the MOI of the spherical shell, as a fraction of the total MOI of the full sphere, is $\alpha_{\mathrm{Sh}} = 0.56$. For the fluid outside the TC, the MOI ratio is $\alpha_{\mathrm{TC}} = 0.4$. However, to obtain an estimate of the MOI ratio for Saturn we need to take into account the increase of density with depth. Saturn's uncertain rotation rate has recently been analyzed using empirical radial density distributions based on *Cassini* gravity data (Helled et al. 2009). The normalized, axial component of the MOI, outside the TC, is derived from the density distribution by the integration

$$\gamma = \frac{C}{M_S R_S^2} = 4\pi \int_{\theta_1}^{\pi/2} \sin^3\theta\, d\theta \int_{\chi_1}^{1} \rho(\chi)\, \chi^4\, d\chi\,, \qquad (12)$$

where θ is the co-latitude, M_S is Saturn's mass, C is the axial MOI, and $\rho(\chi)$ is an empirical five-parameter polynomial representation of the density distribution as a function of the radius ratio $\chi = r/R_S$ (Helled et al. 2009). The integration limit $\theta_1 = \cos^{-1}(\chi_1)$ is the angle at which the axial TC of normalized radius χ_1 intersects the outer spherical surface.

The Saturnian density profile of Helled et al. (2009), along with the results of integrating Equation (7) for all spherical shells of low depth ($(R - r)/R = 0.01$) to a full sphere ($(R - r)/R = 1$) are shown in Figure 9. To estimate γ for Saturn's molecular envelope, we choose a radius r_m that represents the transition from fast, nonmagnetic zonal flow to slow, magnetically controlled flow. Since we propose a planetary tachocline for Saturn to lie within $0.78\ R_S \lesssim r \lesssim 0.88\ R_S$, it seems reasonable to use $\chi_m = r_m/R_S = 0.85$ (which is the radius ratio for our numerical model convective layer). This is shown as a thin vertical line and corresponds to $(R - r)/R = 0.15$ in Figure 9. To obtain an empirical estimate of the MOI of Saturn's entire deep atmosphere outside r_m, Equation (7) is integrated over all latitudes ($0^\circ < \theta < 180^\circ$). However, for the radius ratio $\chi_m = 0.85$ the TC intersects the outer surface at a latitude $90^\circ - \theta_{\mathrm{TC}} = \cos^{-1}(\chi_m) = 32^\circ$. So we use the integration limit from $\theta_1 = \theta_{\mathrm{TC}}$ to obtain the MOI of the deep atmosphere outside the TC. This gives a better estimate of the MOI of fluid mobilized by a convective burst since, in our model, bursts strongly affect only the fluid outside the TC. The resulting estimate of the MOI ratio mobilized by a Saturnian convective burst is $\alpha_{\mathrm{TC}} = \gamma(R_S - r_m)/\gamma(R_S) = 0.11$. In other words, the volume of Saturn's deep atmosphere outside a radius of $r_m = 0.85\ R_S$, and bounded by the TC, carries about 11% of the planetary MOI. If we consider the entire deep atmosphere outside that same radius, the MOI ratio increases to 15% (see Figure 9).

We can now estimate the change in the rotation rate of the interior dynamo in response to a change in the speed of the equatorial jet. Assuming that a Saturnian GWS perturbs the whole volume of fluid outside a TC of radius $r_m = 0.85$, the MOI ratio of the outer fluid is about $\alpha = 0.11$. Thus, conservation of axial angular momentum implies that a

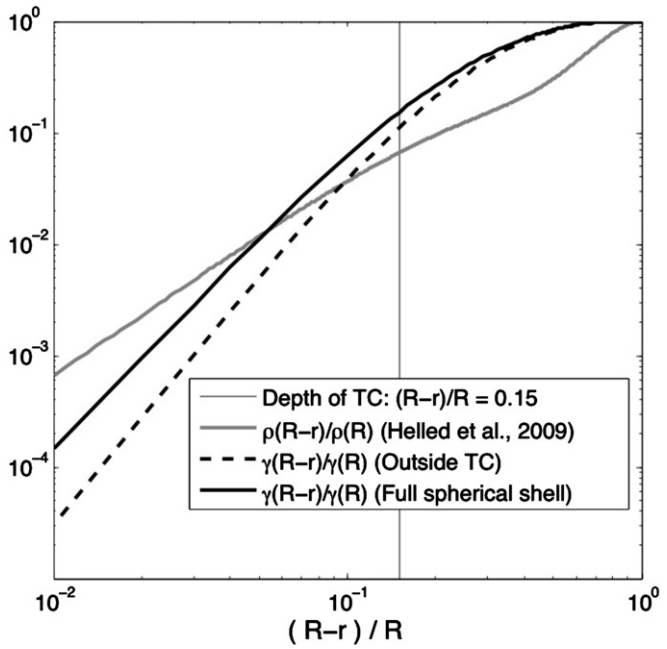

Figure 9. Ratio of the normalized moment of inertia (MOI) of the molecular envelope. The gray line shows the Saturnian density profile (Helled et al. 2009), normalized to the density at $r = 0$, which was used to calculate the MOI. The thick solid line shows the normalized MOI for the entire layer as a function of the layer depth $R - r$. The dashed line shows the MOI of the layer outside the tangent cylinder. The thin vertical line indicates a normalized layer depth of $(R - r)/R = 0.15$, which is an estimate of the maximum depth of fast zonal flow in Saturn.

fractional change in the mean angular velocity of the equatorial jet $\Delta\omega_{\rm jet}/\omega_{\rm jet}$ (where $\omega_{\rm jet}$ is measured with respect to the rotating reference frame) will result in an inertial frame fractional rotation rate change of the interior:

$$\frac{\Delta\Omega_{\rm int}}{\Omega_{\rm int}} \sim -\alpha {\rm Ro}\, \frac{\Delta\omega_{\rm jet}}{\omega_{\rm jet}}, \qquad (13)$$

where the Rossby number ${\rm Ro} = \omega/\Omega$ has a time-averaged value of ${\rm Ro} \sim 0.03$ for Saturn's equatorial jet. So, for example, a 30% increase in the prograde velocity of the equatorial jet would result in a ∼0.1% decrease in the rotation rate of Saturn's interior. This estimate is about 1/10 of the change implied by the roughly 1% variation observed in the SKR signal. To plausibly obtain such a large response, we can consider a scenario in which the SKR signal is seated in a layer of limited thickness, which counterrotates in response to angular momentum changes in the shallower molecular envelope. If such a layer has an MOI similar to, or smaller than, the molecular atmosphere, then a 1% rotation rate change is plausible within this theoretical framework.

4. DISCUSSION

As is the case for all three-dimensional deep convection models, computational resolution requires us to use thermal and viscous diffusion parameters several orders of magnitude greater than those of the giant planets. With our model Ekman number of $E = 10^{-5}$, a Saturnian angular velocity of $\Omega = 1.6 \times 10^{-4}$ s^{-1}, and taking the depth of the semiconducting molecular layer to be $L = 0.15\, R_S = 8.4 \times 10^6$ m, results in a scaled viscosity of $\nu = 1.1 \times 10^5$ m s^{-1}, several orders of magnitude greater than estimates of turbulent diffusivities for the giant planets (e.g., Starchenko & Jones 2002). These high model diffusivities require strong overforcing, with high heat flow, to drive our model at Rossby numbers characteristic of Saturn. However, the high model heat flow (several orders of magnitude higher than planetary values) may not be problematic in terms of interpreting model results in relation to large-scale flows of the giant planets (Jones & Kuzanyan 2009).

It is not straightforward to scale the magnitude nor the frequency of the convective bursts in our models to those of giant planets. As mentioned in Section 1.3, such bursts, which are also known as relaxation oscillations, occur in a variety of Boussinesq and anelastic convective models. In addition, strong and periodic bursts occur with various characteristics and frequencies over a range of Ra in numerical rotating convection models (Grote & Busse 2001). Thus, it seems likely that such phenomena also exist in natural systems.

It can be argued that the existence of convective bursts in giant planets requires the persistence of mean convectively unstable temperature gradients, similar to those of the antipode region in Figure 7(b). Studies have shown that such gradients can indeed persist with increasing Ra in rapidly rotating convection systems. Julien et al. (1996) and Sprague et al. (2006) showed this effect in Cartesian direct numerical simulations and using an asymptotically reduced set of equations, respectively. King et al. (2010) showed the persistence of these gradients in spherical shell planetary dynamo models, finding that the gradients were not strongly sensitive to the strength of the fluid turbulence, parameterized by the Reynolds number Re. Flows that feature quasiperiodic bursts of turbulence have also been found to arise naturally in an experimental study of strongly turbulent spherical Couette flow (Zimmerman et al. 2011). In rapidly rotating ($E \approx 2 \times 10^{-7}$) yet strongly turbulent (Reynolds numbers ${\rm Re} \lesssim 10^6$; Rossby numbers ≈ 2) cases, the higher velocity flow within the TC was found to become unstable, periodically mixing with the full fluid volume. The cycle would then repeat. Taken together, these results support the notion that convective bursts similar to those in our simulations can develop in planets.

If we identify Saturn's 1990 GWS as a convective burst and interpret the decrease in the SKR period since the *Voyager* observations to have resulted from the GWS, we can compare the observations with our numerical model. The origin of GWS events is rather mysterious. Although the historical record of observations is not complete, they seem to occur about every 30 years, corresponding to the Saturnian orbital period, which may imply that seasonal changes in solar heating trigger these events (Sanchez-Lavega et al. 1991). (Our numerical model includes no solar heating, and no seasonal variations. Rather, as noted in Section 1.3, the model convective bursts are relaxation oscillations.) The variability of Saturn's equatorial jet, like the observations of the SKR periodicity, is complex and the subject of ongoing research. For example, it is clear that some of the variability is due to vertical shear in the cloud layers. This means that different viewing instruments, which vary in their spectral sensitivities see different depths, and thus different velocities (e.g., Porco et al. 2005). Furthermore, one effect of the storm, which is not modeled in our simulations, is that the mean elevation of the upper equatorial clouds layer may have changed. Still, observations indicate that at least part of the apparent slowdown of Saturn's equatorial jet is real (Sayanagi & Showman 2007; Gombosi & Ingersoll 2010).

Assuming that there is a link between Saturn's equatorial jet variability and the interior rotation, one of the interesting aspects of the observations is the apparently concurrent post-GWS slowdown of both the prograde jet velocity and the SKR signal (i.e, the apparent interior rotation rate). In our numerical model, an increase in the mean equatorial jet speed is preceded

by a decrease of the equatorial flow speed near the outer boundary, which occurs on a very short timescale, and is easily explained by the direct effect of the Coriolis force acting on fluid traveling up and away from the rotation axis. We propose that the following process can explain the decrease in Saturn's surface flow post-GWS. In our simulation, and on a longer timescale (hundreds of rotations), Reynolds stress spins up the net angular momentum of the equatorial jet (i.e., the volume of fluid outside the TC). This results in a slowdown of the inner rigid sphere (via viscous torques), and a reversal of the flow acceleration near the outer boundary. Thus, the earlier slowdown of the equatorial surface jet is followed by an increase in the prograde surface velocity.

A similar sequence, but with a different detailed chronology may be occurring in Saturn after the GWS. The key difference between our simulation and Saturn may be due to variation of spin-up times in the Saturnian molecular envelope. We have argued in Section 3 that the zonal wind region is governed by the viscous, or turbulent spin-up time τ_E, while the deep interior is likely governed by the magnetic spin-up time τ_A (see Equations (5) and (6)). Near the bottom of the zonal wind layer the magnetic diffusivity is of order 10^6 m^2 s^{-1}, which is much greater than any reasonable eddy viscosity (Starchenko & Jones 2002). Thus, with increasing depth in the molecular envelope, the spin-up timescale increases rapidly near the bottom of the zonal wind layer. Again, we may call this region of strong gradients in effective diffusivity and velocity the planetary tachocline. Since the spin-up time near the tachocline is much shorter than that near the cloud layer, we would expect Reynolds stresses to act on a short timescale deep in the atmosphere and on a longer timescale near the surface. This implies that, in response to the GWS (convective burst), the deep atmosphere can be spun up in the prograde direction while a slowdown (due to the direct Coriolis effect) is observed for the surface flow.

5. CONCLUSIONS

Our numerical model shows that deep convective bursts can mobilize zonal flows, change the angular momentum of the convective region, and thus change the rotation rate of the interior. Variations of the zonal flow near the outer boundary of our model occurs in two stages. First, the equatorial jet slows down by about 10%. During this stage angular momentum of the convective fluid is roughly conserved such that there are no significant changes in the rotation rate of the inner sphere. Next, Reynolds stress acts on the fluid to increase the mean prograde velocity of the surface flow at the equator by about 50%. The mean increase in the prograde angular momentum is matched by a decrease in the rotation rate of the inner sphere by 0.035%.

Using empirical radial density profiles (Helled et al. 2009), we calculate the MOI of Saturn's molecular envelope down to an estimated maximum depth of fast zonal flow (at $\simeq 0.85\,R_S$) is $\simeq$15% of the global MOI. The MOI of the sub-volume of the layer outside the TC of radius $\sim 0.85\,R_S$ for Saturn is $\simeq$11%. For Jupiter, the corresponding layer (down to $\simeq 0.95\,R_J$) and the subvolume outside the TC carry $\simeq$0.01% and $\simeq$0.005% of the global MOI, respectively.

Scaling of the forces that act on the azimuthal flows in the giant planets implies the existence of a thin and dynamically anomalous transition layer, which may be referred to as the planetary tachocline. The planetary tachocline is estimated to lay within the molecular envelope, at the bottom of the layer of fast zonal flow, roughly centered in depth between the cloud deck and the top of metallic core. This layer is characterized by strong gradients in electrical conductivity and flow velocity, and a correspondingly strong Lorentz force, which implies that the Alfvén wave crossing time τ_A, is important in the spin-up dynamics. The relative strength of Coriolis forces is stronger at the poles than at the equator. As a result, the spin-up timescale of the planetary tachocline, and perhaps its thickness or shape, is likely to depend on latitude as well.

Taken together, our numerical models and scaling results suggest that Saturn's great equatorial storms, including the GWS of 1990, can be described as planetary convective bursts that can generate enough angular momentum to cause significant rotational disturbances in a magnetically rigid layer that may be referred to as the planetary tachocline. Assuming a planetary tachocline with an MOI similar to or less than that of the zonal flow layer, it is plausible that the Saturn's GWS has caused the significant ($\simeq$1%) changes in SKR periodicity, which originate in planet's magnetic source region and may be seated partially or wholly in a planetary tachocline.

The authors thank the anonymous referee for insightful comments and suggestions that have improved the quality of this work. M.H. was funded by an NSERC Discovery grant. J.M.A. was funded by a NASA PATM grant. Computational resources were provided by Western Canada Research Grid (WestGrid) and Réseau québécois de calcul de haute performance (RQCHP).

REFERENCES

Anderson, J. D., & Schubert, G. 2007, Science, 317, 1384
Aurnou, J., Heimpel, M., Allen, L., King, E., & Wicht, J. 2008, Geophys. J. Int., 173, 793
Aurnou, J., Heimpel, M., & Wicht, J. 2007, Icarus, 190, 110
Aurnou, J. M., & Olson, P. L. 2001, Geophys. Res. Lett., 28, 2557
Ballot, J., Brun, A. S., & Turck-Chieze, S. 2007, ApJ, 669, 1190
Benton, E. R., & Loper, D. E. 1969, J. Fluid Mech., 39, 561
Berdyugina, S., & Usoskin, I. 2003, A&A, 405, 1121
Braginsky, S. I. 1970, Geomagn. Aeron., 10, 1
Brito, D., Aurnou, J., & Cardin, P. 2004, Phys. Earth Planet. Inter., 141, 3
Brown, B. P., Browning, M. K., Brun, A. S., Miesch, M. S., & Toomre, J. 2008, ApJ, 689, 1354
Brummell, N. H., Hurlburt, N. E., & Toomre, J. 1998, ApJ, 493, 955
Brun, A. S., & Toomre, J. 2002, ApJ, 570, 865
Busse, F. H. 1976, Icarus, 20, 255
Busse, F. H. 2002, Phys. Fluids, 14, 1301
Christensen, U., & Aubert, J. 2006, Geophys. J. Int., 166, 97
Christensen, U., Olson, P., & Glatzmaier, G. 1999, Geophys. J. Int., 138, 393
Christensen, U. R. 2001, Geophys. Res. Lett., 28, 2553
Christensen, U. R. 2002, J. Fluid Mech., 470, 115
Christensen, U. R., Schmitt, D., & Rempel, M. 2009, Space. Sci. Rev., 144, 105
Christensen, U. R., & Wicht, J. 2007, in Treatise on Geophysics, Vol. 8, ed. P. L. Olson (Amsterdam: Elsevier), 245
Deleplace, B., & Cardin, P. 2006, Geophys. J. Int., 167, 557
Fischer, G., Kurth, W. S., Gurnett, D. A., et al. 2011, Nature, 475, 75
Galloway, D. J., Proctor, M. R. E., & Weiss, N. O. 1977, Nature, 266, 686
Giampieri, G., Dougherty, M. K., Smith, E. J., & Russell, C. T. 2006, Nature, 441, 62
Gillet, N., Jault, D., Canet, E., & Fournier, A. 2010, Nature, 465, 74
Glatzmaier, G. A. 1984, J. Comput. Phys., 55, 461
Glatzmaier, G. A. 2002, Annu. Rev. Earth Planet. Sci., 30, 237
Glatzmaier, G. A. 2008, Icarus, 196, 665
Gombosi, T. I., & Ingersoll, A. P. 2010, Science, 327, 1476
Gómez-Pérez, N., & Heimpel, M. 2007, Geophys. Astrophys. Fluid Dyn., 101, 371
Greenspan, H. P., & Howard, L. N. 1963, J. Fluid Mech., 17, 385
Grote, E., & Busse, F. H. 2001, Fluid Dyn. Res., 28, 349
Guillot, T. 1999, Science, 286, 72
Guillot, T., Stevenson, D. J., Hubbard, W., & Saumon, D. 2004, in Jupiter, the Planet, Satellites and Magnetosphere, ed. F. Bagenal, T. Dowling, & W. McKinnon (Cambridge: Cambridge Univ. Press), 35

Gurnett, D. A., Lecacheux, A., Kurth, W. S., et al. 2009, Geophys. Res. Lett., 36, L16102
Heimpel, M., & Aurnou, J. 2007, Icarus, 187, 540
Heimpel, M., Aurnou, J., & Wicht, J. 2005, Nature, 438, 193
Heimpel, M., & Gómez Pérez, N. 2011, Geophys. Res. Lett., 38, L14201
Helled, R., Schubert, G., & Anderson, J. D. 2009, Icarus, 199, 368
Hollerbach, R. 2000, Int. J. Numer. Methods Fluids, 32, 773
Jones, C. A. 2007, in Treatise on Geophysics, Vol. 8, ed. P. Olson (Amsterdam: Elsevier), 131
Jones, C. A., & Kuzanyan, K. M. 2009, Icarus, 204, 227
Jones, C. A., Thompson, M. J., & Tobias, S. M. 2010, Space Sci. Rev., 152, 591
Julien, K., Legg, S., McWilliams, J., & Werne, J. 1996, J. Fluid Mech., 322, 243
Kaspi, Y., Flierl, G. R., & Showman, A. P. 2009, Icarus, 202, 525
King, E., Soderlund, K., Christensen, U., Wicht, J., & Aurnou, J. 2010, Geochem. Geophys. Geosyst., 11, Q06016
Kirk, R. L., & Stevenson, D. J. 1987, ApJ, 316, 836
Lian, Y., & Showman, A. 2008, Icarus, 194, 597
Liu, J., Goldreich, P. M., & Stevenson, D. J. 2008, Icarus, 196, 653
Liu, J., & Schneider, T. 2010, J. Atmos. Sci., 67, 3652
Liu, J. J. 2006, PhD thesis, California Institute of Technology
Loper, D. E., & Benton, E. R. 1970, J. Fluid Mech., 43, 785
Miesch, M., Brun, A., & Toomre, J. 2006, ApJ, 641, 618
Nellis, W. J., Weir, S. T., & Mitchell, A. C. 1996, Science, 273, 936
Nellis, W. J., Weir, S. T., & Mitchell, A. C. 1999, Phys. Rev. B, 59, 3434
Nettelmann, N., Holst, B., Kietzmann, A., et al. 2008, ApJ, 683, 1217
Olson, P., & Christensen, U. R. 2006, Earth Planet. Sci. Lett., 250, 561
Porco, C. C., Baker, E., Barbara, J., et al. 2005, Science, 307, 1243
Read, P. 2011, Nature, 475, 44
Rempel, M. 2005, ApJ, 622, 1320
Roberts, P. H. 2007, in Treatise on Geophysics, Vol. 8, ed. P. L. Olson (Amsterdam: Elsevier), 67
Rotvig, J., & Jones, C. A. 2002, Phys. Rev. E, 66, 056308
Russell, C. T., & Dougherty, M. K. 2010, Space Sci. Rev., 144, 105
Salpeter, E. E. 1973, ApJ, 181, L83
Sanchez-Lavega, A. 2005, Science, 307, 1223
Sanchez-Lavega, A., Colas, F., Lecacheux, J., et al. 1991, Nature, 353, 397
Sanchez-Lavega, A., del Río-Gaztelurrutia, T., Hueso, R., et al. 2011, Nature, 475, 71
Sanchez-Lavega, A., Perez-Hoyos, S., Rojas, J. F., Hueso, R., & French, R. G. 2003, Nature, 423, 623
Sanchez-Lavega, A., Rojas, J. F., & Sada, P. V. 2000, Icarus, 147, 405
Sayanagi, K. M., & Showman, A. P. 2007, Icarus, 187, 520
Schneider, T., & Liu, J. 2009, J. Atmos. Sci., 66, 579
Schou, J., Antia, H. M., Basu, S., et al. 1998, ApJ, 505, 390
Showman, A., Gierasch, P., & Lian, Y. 2006, Icarus, 182, 513
Southwood, D. J., & Kivelson, M. G. 2007, J. Geophys. Res., 112, A12222
Sprague, M., Julien, K., Knobloch, E., & Werne, J. 2006, J. Fluid Mech., 551, 141
Stanley, S., & Glatzmaier, G. A. 2010, Space Sci. Rev., 152, 617
Stanley, S., & Mohammadi, A. 2008, Phys. Earth Planet. Inter., 168, 179
Starchenko, S. V., & Jones, C. A. 2002, Icarus, 157, 426
Stevenson, D. 2003, Earth Planet. Sci. Lett., 208, 1
Stevenson, D. J. 1982, Annu. Rev. Earth Planet. Sci., 10, 257
Tilgner, A., & Busse, F. 1997, J. Fluid Mech., 332, 359
Wicht, J. 2002, Phys. Earth Planet. Inter., 132, 281
Yano, J. I., Talagrand, O., & Drossart, P. 2003, Nature, 421, 36
Zhang, C. 2005, Rev. Geophys., 43, RG2003
Zimmerman, D. S., Triana, S. A., & Lathrop, D. P. 2011, Phys. Fluids, 23, 065104